Available online at www.sciencedirect.com
SCIENCE DIRECT®
PERGAMON
International Journal of Heat and Mass Transfer 46 (2003) 4845–4862
International Journal of HEAT and MASS TRANSFER
www.elsevier.com/locate/ijhmt

Heat transfer of impinging air and liquid nitrogen mist jet onto superheated flat surface

L.M. Su [a], S.W. Chang [b,*], C.I. Yeh [b], Y.C. Hsu [b]

[a] *Department of Electrical Engineering, Tung Fang Institute of Technology, No. 110, Tung Fang Road, Hu-Nei Shang Kaohsiung Hsien, Taiwan, ROC*

[b] *Department of Marine Engineering, National Kaohsiung Institute of Marine Technology, No. 142, Hai-Chuan Road, Nan-Tzu District, 811 Kaohsiung, Taiwan, ROC*

Received 1 May 2002; received in revised form 6 May 2003

Abstract

This experimental study performs the detailed heat transfer measurements of an impinging air–liquid nitrogen mist jet onto a superheated flat surface at atmospheric pressure with reference to the design of an instant freezing facility. A selection of experimental results illustrates the interacting effects of jet Reynolds number, mass flow ratio of air to liquid nitrogen flows and separation distance on the spatial distributions of heat transfer over the impinging surface. Mechanism associated with phase change of impacting droplets generates an enhanced and uniformly distributed heat transfer region centered on the stagnation point. A narrow oval-ring region encapsulating the enhanced core transits heat transfer from the wetting regime of complete evaporation to the non-wetting rebound regime. Stagnation heat transfer augmentation factor in the range of 1.2–2.8 times of the air-jet level is achieved. An empirical correlation based on the experimental data, which is physically consistent, has been developed to permit the evaluation of stagnation heat transfer.

Keyword: Impinging air–liquid nitrogen mist jet heat transfer

1. Introduction

Taiwan's earthquake on 21st September 1999 exposes the urgent requirement for the freezing source, which is portable, electricity-free and can be kept in stores for emergency usages of medical treatment and food processing. Spray cooling by a flow of air containing droplets of liquid nitrogen is of great interest in the above application as the required air and liquid nitrogen could be readily collected from the tanks in stores. Such spray cooling offers an opportunity to attain freezing capability at atmospheric pressure level with the higher heat transfer rates opposed to those of conventional single-phase convective flows. The advantage of liquid nitrogen capable of phase-change at freezing temperatures, which leads to heat transfer enhancement, motivates the present investigation.

The liquid droplets possess the relatively high inertia gaining from the air streamlines to strike directly against the heated surface in the atomized spray. Upon impacting either directly on the solid surface or on the liquid film over the target surface, the droplets could stick, rebound, spread or splash. The droplet-wall impacting dynamics could be the most dominant mechanism in the dilute spray system, which depends strongly on the droplet impinging velocity, angle of incidence, splashing effects and the size spectrum of droplets [1–3]. In dense sprays, the droplet-wall heat transfer is not considerably influenced by the droplet impacting dynamics but is affected by the liquid mass flux alone [2]. When the mass flux of liquid in an impinging spray reaches the high end of dense spray region, a scenario of boiling/evaporative wetting evolves which is characterized by the formation of a thin liquid film around the

* Corresponding author. Fax: +86-886-7-5712219.
E-mail address: swchang@mail.nkimt.edu.tw (S.W. Chang).

0017-9310/$ - see front matter © 2003 Elsevier Ltd. All rights reserved.
doi:10.1016/S0017-9310(03)00319-3

Nomenclature

C	specific heat of heating foil (J/kg K)
Cp	specific heat of air (J/kg K)
D_j	hydraulic diameter of jet (m)
D_s	downward shift length of mist jet due to gravity (m)
h	heat transfer coefficient, $q/(T_w - T_j)$ (W/m^2 K)
h_{fg-N_2}	latent heat of liquid N_2 at ambient pressure level (J/kg)
h_{loss}	heat loss coefficient (W/m^2 K)
L	thickness of heating foil (m)
$\dot{m}^A$	air mass flow rate issued from jet (kg/s)
$\dot{m}^N$	liquid nitrogen mass flow rate issued from jet (kg/s)
q	convective heat flux (W/m^2)
q_g	total heat flux generated (W/m^2)
Re	Reynolds number
S	separation distance (m)
T_a	air jet entry temperature (°C)
T_j	fluid temperature at exit of nozzle (°C)
T_w	wall temperature (°C)
T_{wi}	initial wall temperature for heat loss calibration test (°C)
T_{sat}	saturated temperature of liquid nitrogen at ambient pressure (°C)
T_∞	ambient temperature (°C)
X, Y	dimensionless location ($x/D_j, y/D_j$)

Greek symbols

ρ	density of heating foil (kg/m^3)
μ	fluid dynamic viscosity of air (kg/m s)
θ_c	spread angle of spray (degree)
θ_s	downward shifting angle of mist jet, $\tan^{-1}(D_s/S)$ (degree)
χ	wetting fraction of air/liquid nitrogen mist jet at exit of atomizing nozzle (%)
Ψ, ξ	unknown functions

Superscripts

A	air jet
N	air/liquid nitrogen mist jet

Subscript

S	stagnation point of jet

stagnation point. The droplets upon impinging heated surface form a liquid film over the solid wall whose thickness can be much lower than the diameters of droplet [4]. On the top of this liquid film that can be about 10–50 μm thick [5], the air stagnation flow field entrains ambient fluid into the jet stream. The liquid film flow is then driven by the superjacent wall-jet airflow directed radially outward. If the liquid flow rate before entering the spray nozzle increases, both the liquid velocity and the liquid film thickness increase [6]. The studies of impinging mist jet onto a sub-cooled heating surface could isolate the effects of interacting boiling mechanism from the heat transfer physics [6–8]. Three different heat transfer mechanisms, namely the region I: convective heat transfer of stagnation airflow; the region II: evaporative heat removal at the air/liquid interface and, possibly; the region III: laminar-like convection of liquid-film flow facilitate the overall heat removal capability of an impinging spray over a sub-cooled surface. The net result of heat transfer performance for an impinging mist jet onto a sub-cooled heating surface is a trade-off between competing influences of these three different heat transfer components.

The evaporation of the droplets impinging upon a superheated surface through the phase change process considerably added the overall heat removal and hence results in heat transfer enhancement [2,9–12]. Quite different mechanisms dominate the overall heat removal capability for the dilute and dense sprays [2,9]. When a droplet in the dilute spray approaches the superheated wall, a repulsive force generated by an extensive pressure inside vapor bubbles or in a thin vapor interlayer separates the droplet from the wall. If the overheat of wall is small, the approaching droplet is capable of penetrating the vapor region to make direct contact with wall. When overheat exceeds a critical level, the droplet dynamics change radically: the spreading out and subsequent evaporation, which is accompanied by the elastic rebound without appreciable contribution for heat removal from the solid wall. Consequently the non-wetting regime replaces the wetting one around the stagnation point [11]. Three distinct heat transfer regions for dilute spray over superheated surface, namely the nucleate boiling region, the transition with considerable reduction in heat flux, and the film boiling region are subsequently developed when the difference between wall temperature and the equilibrium boiling temperature of the dispersed liquid increases [2,9]. In the nucleate boiling region, the efficient absorption of latent heat from the heated wall takes place and any vapor that emanates from the superheated surface is swept away by the bulk convective flow, which enhances evaporation even further by reducing the partial vapor pressure [10]. With wall temperature beyond the Leidenfrost level, film boiling occurs such that the liquid could be separated from the impinging surface by a vapor cushion. The

contact heat transfer becomes less effective than the case of nucleate boiling as the droplets could be bounced back upon impacting on the vapor cushion. A region that transits better heat transfer capability from nucleate boiling towards the film boiling develops in the overheat range of about 30–150 °C [9]. With dense spray that the evaporation/boiling at the film surface is completely compensated by the incessant liquid supply from the mist jet, the heat transfer physics bear the resemblance of pool or convective boiling scenarios [2,11]. Dense spray heat transfers do not show much dependence on the droplet diameter and velocity because possibly that the strong droplet interaction effects suppress the droplet dynamics. In the limit of reaching the pooling boiling condition, heat transfer is completely independent of droplet characteristic [2]. A liquid mass flux of about 2 $kg\,m^{-2}\,s^{-1}$ could be regarded as a comprehensive guideline to characterize water sprays impinging on a stainless steel surface as dilute or dense [2].

Also play an important role in an impinging spray is the promoting mixing of free stream turbulence for stagnation air flow due to the large-scale pulsations penetrating the boundary layer that leads to considerable heat transfer enhancement in bulk-air convection [2,13,14]. The mutually correlated dynamic interactions between the evaporating/impacting liquid nitrogen droplets, the stagnation airflow and the surface evaporation/boiling feature a complex heat transfer phenomenon. This experimental investigation attempts a parametric strategy to study the overall heat transfer performance of an impinging air–liquid nitrogen spray for a set of pre-defined geometrical and thermal boundary conditions. The individual and interactive influences of jet Reynolds number, mass fluxes of air and liquid nitrogen flows and the separation distance on the detailed spatial heat transfer distributions over the impinging surface are systematically examined with the attempt to devise an empirical correlation for evaluating the stagnation heat transfer.

2. Experimental details

2.1. Apparatus

The experimental apparatus is shown in Fig. 1. The dehumidified and pressurized air is directed via a flow calming section (1) with equivalent straight length of 300 mm into a Teflon-made cylindrical settling chamber (2), and ejects from the atomized nozzle (3). The atomized nozzle (3) and the heating surface are arranged so that the mist jet impinges horizontally and is perpendicular to gravity. This arrangement attempts to avoid the secondary impactions of the splattered droplets after the first impaction on the target plate. The influence of gravity on the motions of droplet, wall-jet flow, and liquid film, which causes consequent effect on heat transfer, is considered when the spray impinges horizontally. As illustrated in the sectioned view of the atomized nozzle (3), the exit region of convergent air-jet nozzle is encapsulated within a "ring-shaped chamber" in which the liquid nitrogen is fed from the thermally insulated vessel (4). Four 1-mm holes drills radially through the air-jet nozzle. When the dry airflow traverses the convergent nozzle with high velocity, the liquid nitrogen from the annulus is entrained within the airflow to generate the air/liquid nitrogen mist spray. The exit diameter of the atomizing

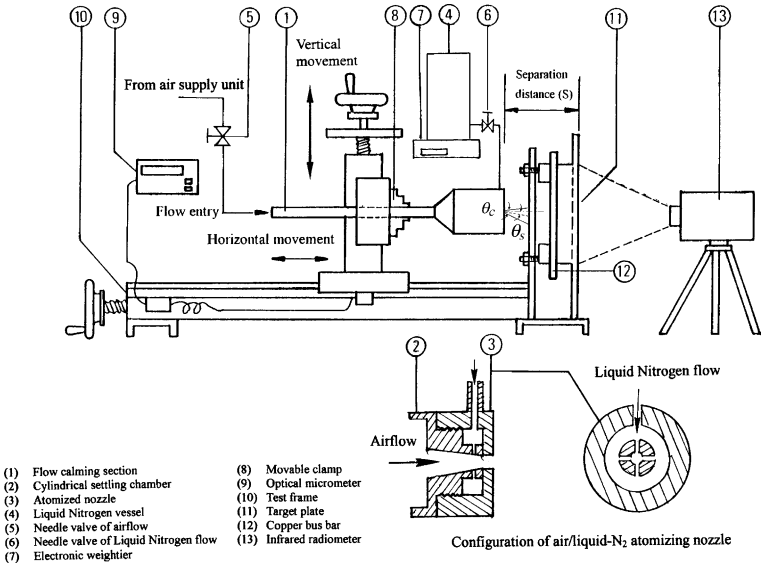

Fig. 1. Schematics of experimental apparatus.

nozzle, D_j, is 5 mm. By controlling the needle valves of the airflow and liquid nitrogen flow (5) and (6) respectively, the mass flow rate of liquid nitrogen entrained into the airflow is adjusted. Note that, as the geometrical feature of the atomized nozzle (3) is predefined, the size spectrum and velocity of droplet vary inter-dependently on the mass fluxes of air and liquid nitrogen. Alternatively, once the air-jet Reynolds number, the mass flux of liquid nitrogen and the separation distance from the nozzle exit to the target plate are controlled, the interactions of droplets before and upon impaction could be reproduced. To measure the mass consumption of liquid nitrogen, the complete assembly of thermally insulated vessel (4) that stores liquid nitrogen is positioned on a digital-type electronic weightier (7) with precision of 0.01 g. Over any period of time, the mass consumption of liquid nitrogen measured by the electronic weightier (7) is converted into the mass flow rate of liquid nitrogen.

Prior to entering the flow calming section (1), the air fed form the IWATA SC 175C screw-type compressor unit is dehumidified and cooled to the controlled temperature of 25 °C through a refrigerating unit that is integrated with the compressor. The dry and cooled airflow is then guided through a set of pressure regulator and filter with the mass flow rate to be metered and adjusted by a Tokyo Keiso TF-1120 mass flow meter and a needle valve respectively. The complete jet assembly is secured and centered on a movable clamp (8). The vertical and horizontal movements of this clamp (8) are adjusted by two independent thread mechanisms, which could be precisely adjusted in order to center the jet and to control the separation distance. Note that, it shows a tendency that the downward shift of air/liquid nitrogen mist jet decreases when the Reynolds number of mist jet increases. The vertical movement is required to center the impinging mist jet onto the target plate. An optical micrometer (9) with the precision of 0.01 mm is mounted on the test frame (10) to measure the separation distance from the target plate (11). The impinging surface of the target plate (11) is polished to a mirror finish. With the assistance of the precision provided by the optical micrometer, the separation distance, S, could be precisely controlled. The jet issued from the atomizing nozzle (3) impinges horizontally against a very thin (0.1 mm) and 120 mm wide stainless steel foil (11). This heating foil (11) is stretched tightly between two copper bus bars (12). The adjustable high current DC electrical power directly feeds into the steel foil (11) to generate the basically uniform heat flux surface. The foil deflection and dimpling under the maximum Reynolds number tested at separation distance of four jet diameter is less than 0.01 mm as measured by a precision caliper. The temperatures of the heating surface under each test condition are imaged by a two-dimensional NEC TH3101-MR infrared radiometer (13). For this thermal image processing system, it takes 0.3 s to complete a full field of 239×255 matrix scan. The back surface of the heating foil (11) is painted flat black in order to minimize the background reflection and to increase the emission. An additional type K thermocouple is used to measure the ambient temperature that is required to evaluate the external "heat loss".

2.2. Program and procedures

The experimental program involves two phases. Initially the heat transfer distribution over the impinging surface of air jet is checked out with a series of baseline tests over a range of separation distances of 4, 6, 8 and 10 jet diameters and Reynolds numbers of 5000, 10,000, 15,000 and 20,000. The range of Reynolds numbers tested ensures the turbulent jets because the jet becomes turbulent with $Re \geqslant 3000$ [15]. This phase of tests is followed by a similar series of experiments using air/liquid nitrogen mist jet. With the same test ranges of Reynolds number and separation distance, the heat transfer results generated from the two phases are compared to reveal the heat transfer modifications caused by the air/liquid nitrogen impinging mist jet.

When the droplets of liquid nitrogen travel downstream in the far region of mist jet toward the impinging surface, they entrain the surrounding air and induce the complex interactions between the droplets of liquid nitrogen and airflow. The evaporation process of liquid nitrogen also prevails over the near and far regions of atomizing spray at the ambient pressure level before the droplets of liquid nitrogen hit the superheated surface. Certain portion of latent heat for droplet of liquid nitrogen to evaporate is obtained from the airflow in the spray so that the dryness of liquid nitrogen increases. This process allows the temperature of mist jet dropping to the saturated temperature of liquid nitrogen corresponding to the ambient pressure level. A portable type K thermocouple constantly checks this saturated temperature of air/liquid nitrogen mist jet at the exit of atomized nozzle. If the entrainments from the surrounding atmosphere of spray is not considered, the embodiment of first law of thermodynamics for the mixing process between the gas and liquid phases in the atomizing spray nozzle enables the approximation of wetting fraction of liquid nitrogen as

$$\chi = 1 - \frac{\dot{m}_{\mathrm{air}} Cp(T_{\mathrm{a}} - T_{\mathrm{sat}})}{\dot{m}^{\mathrm{N}} h_{fg-\mathrm{N}_2}} \tag{1}$$

where T_{a} is the air temperature before the mixing process initiates. A review of the complete set of experimental data shows that the dryness of liquid nitrogen is less than 0.02 over the ranges of separation distance and Reynolds numbers tested. The mass flux of liquid nitrogen is above 20 $\mathrm{kg\,m^{-2}\,s^{-1}}$ at the exit of nozzle, which

level is well in excesses of 2 $kg\,m^{-2}\,s^{-1}$ so that the present spray investigated falls into the high end of dense spray [2].

For each individual test, the apparatus is allowed to achieve steady state. A steady state is assured when the variations of wall temperatures over the impinging surface are less than 0.3 °C for each test at the predefined flow condition and heating power. The on-line infrared thermal-image data capture system is then activated to transfer the full field wall temperature measurements over the impinging surface into a raw data file for subsequent data processing. Along with the measured heating power and jet temperature, T_j, the distributions of heat transfer coefficients over the impinging surface at the prescribed Reynolds number and separation distance are evaluated. With tests at each $Re - S/D_j$ option, the heater powers are adjusted to maintain the stagnant wall temperatures at −15 °C. This generally fixed the superheated temperature of $T_w - T_{sat}$ at about 180 °C for the air/liquid nitrogen spray. Note that, although the superheated temperatures at the stagnant point for all the tests are controlled at about 180 °C, it is still infeasible to control the entire superheated levels over the impinging surface at the precise values owing to the spatial variations of flow field and boiling conditions over the heated surface when the jet Reynolds number or separation distance varies. This overheating level brings the impinging spray falling into the film boiling regime, within which the heat transfer appears to be weak function of overheat [2,9]. When the flow and geometrical features, such as the air jet Reynolds number, the mass flux of liquid nitrogen and the separation distance are selected, the flow field accompanying with evaporation/boiling mechanism of liquid nitrogen over the impinging surface is generated. The influences of varying the air jet Reynolds number, mass flux of liquid nitrogen and separation distance on heat transfer are examined.

To evaluate the local heat transfer coefficient over the impinging surface, the convective heat flux, q, is calculated from the electrical dissipation measured over the entire heating surface with the "heat loss" to be subtracted. When the droplets of liquid nitrogen impinge onto the overheated surface, the resultant local wall temperatures on the heated impinging surface could be higher or less than the ambient temperatures. The external heat could be either convected into or out of the heated foil from the backside of the impinging surface. It is thus required to predetermine the heat loss coefficients for both conditions with the wall temperatures higher and less than the ambient levels through a number of heat loss calibration runs. When the wall-to-ambient temperature differences are negative, the external heat is convected into the impinging surface. It is difficult to measure the local heat flux transferred into the target foil if the heat loss coefficient is to be evaluated using the traditional steady-state method. Alternatively, the heat loss coefficient is evaluated using the transient method developed in [8]. For each set of calibration runs, the impinging surface could be either initially heated up or cooled by feeding heating power or by ejecting air/liquid nitrogen mist jet without heating respectively. After the initial wall temperature reaches the predefined level, the heating power is switched off and the air/liquid nitrogen mist jet is blocked off. Under such circumstance, the temporal wall temperature variations are entirely controlled by the natural convections over the two exposed faces of the target foil. As the wall temperatures on both sides of the vertical foil are the same, the identical natural convective coefficients on both sides of the vertical foil are assumed. When the initial wall temperature is lower (higher) than the ambient temperature, the wall temperature gradually increases (decreases) over a fixed time interval during each heat loss calibration run. The higher heat loss coefficient is reflected by a larger temperature variation with the fixed time interval, t. The external heat loss coefficient, h_{loss}, is evaluated using Eq. (2) [8]:

$$\frac{T_w - T_{wi}}{T_\infty - T_{wi}} = 1 - e^{-h_{loss}t/\rho CL} \tag{2}$$

All symbols appeared in Eq. (2) are referring in the nomenclature section. Fig. 2a shows the variations of heat loss coefficient, h_{loss}, against the wall-to-ambient temperature difference for both "overheated" and "sub-cooled" conditions. The data trends shown in Fig. 2a for both overheated and sub-cooled regions indicate the zero asymptotic heat loss coefficients when the wall-to-ambient temperature difference approaches zero. In both overheated and sub-cooled regions, the heat loss coefficient, h_{loss}, increases with the wall-to-ambient temperature difference. Note that the relatively moderate variation of heat loss coefficient, h_{loss}, against wall-to-ambient temperature difference is found in the overheated region. The natural convective heat loss with sub-cooled condition is greater than the corresponding overheated condition although the wall-to-ambient temperature difference remains at the same value. Two equations correlated from the heat loss experiments, which respectively calculate the heat loss flux for overheated and sub-cooled conditions, are incorporated into the data processing program to evaluate the local heat flux convected by the flow. The jet temperatures, T_j, for the air and air/liquid nitrogen jet are constantly checked out using a portable thermocouple penetrated into the jet core. A review of the entire set of experimental raw data reveals that the differences between the saturated temperatures of liquid nitrogen at the measured ambient pressures and the measured jet temperature, T_j, are less than 0.36%. The local heat transfer coefficient is evaluated as

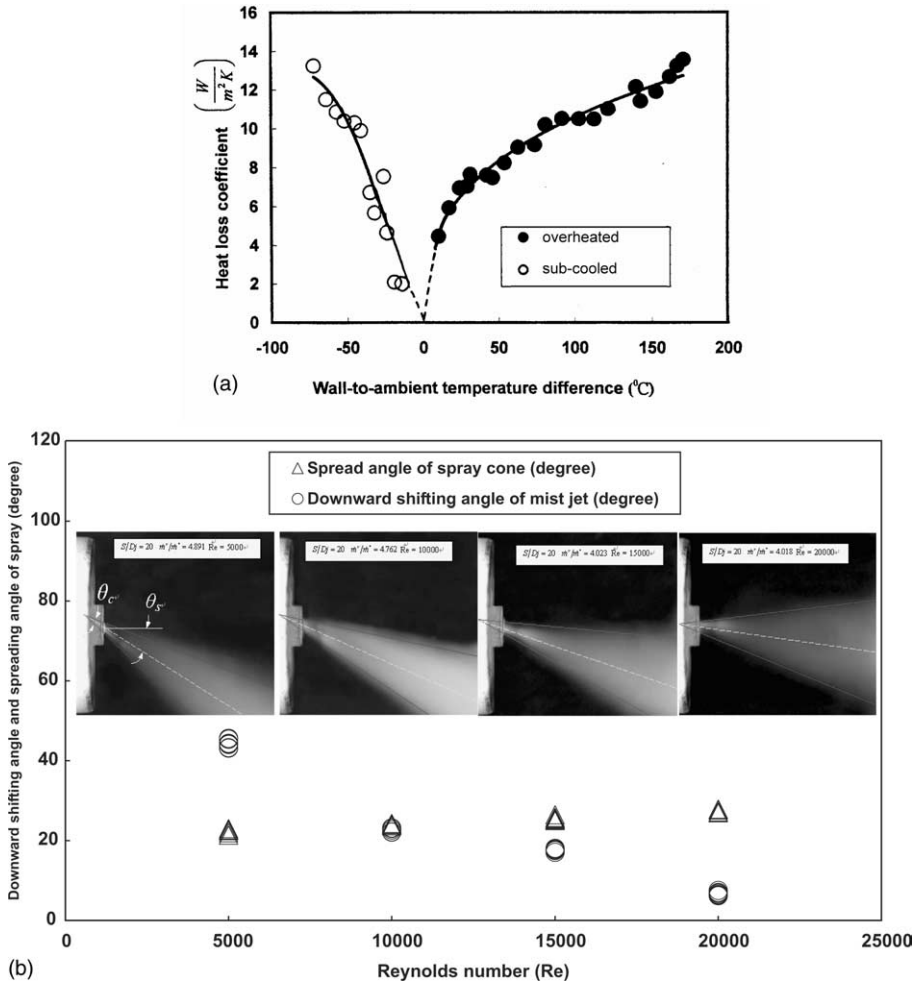

Fig. 2. Heat loss characteristics and variations of spread angle and downward shifting angle of spray with Reynolds number.

$$h = \frac{q_g - h_{loss}(T_w - T_\infty)}{T_w - T_j} \tag{3}$$

Also worth noting that, based on the conventional photographic technique and the thermal images captured by the infrared data acquisition system, the measurements of spread angles of spray cone, θ_c, and the vertical shifts of jets due to gravity are respectively performed. The measurement of vertical shift of air–N_2 mist jet due to gravity is undertaken using the infrared thermal image system. To perform such tests for measuring the vertical shift distance of mist jet due to gravity, the impinging surface is heated with the pure air jet to be initially issued from the nozzle. The stagnation point on the heated surface could be readily identified from the thermal image captured, which point is treated as the reference coordinate for evaluating the vertical shift distance of mist jet due to gravity. When the air and liquid nitrogen mist jet is issued from the nozzle, the downward shift of stagnation point is clearly observed in the thermal image of impinging surface. The adjustment of vertical movement using the mechanism illustrated in Fig. 1, which compensates the vertical shift of stagnation point from the pure air-jet reference point, reveals the shifting distance of mist jet due to gravity. This vertical shift is subsequently normalized by the separation distance to acquire the angle of downward shift of mist jet, θ_s, for each flow condition examined having different values of $\dot{m}^N/\dot{m}^A$, Re and S. Fig. 2b shows the varying manners of the spread angle of spray cone, θ_c, and the downward shifting angle of mist jet, θ_s, in the Reynolds number range of 5000–20,000. As shown in Fig. 2b, the tightened data bands observed at each measured Reynolds number are generated by different separation distances and mass flow ratios, $\dot{m}^N/\dot{m}^A$, tested. The data convergence observed at each Reynolds number showed

in Fig. 2b confirms the weak dependency of θ_c and θ_s on S/D_j and $\dot{m}^N/\dot{m}^A$. The spread angle of spray cone and the downward shifting angle of mist jet respectively increases and decreases when the Reynolds number increases as shown in Fig. 2b.

To evaluate jet Reynolds number, the coolant viscosity is determined from the air temperature measured by an additional type K thermocouple positioned in the air plenum chamber. The experimental repeatability of temperature measurement using NEC TH3101-MR infrared radiometer is checked out for the baseline air jet experiment. The maximum variations of wall temperature measurements with the flows to reach the same steady state conditions are in the range of ±0.7 °C for the present system. Thus the maximum uncertainty of temperature measurement is estimated as ±0.7 °C, which contributes the major source of uncertainties for the coolant's thermal conductivity, fluid density and viscosity. Following the policy of ASME on reporting the uncertainties in experimental measurements and results [16], the maximum uncertainty associated with the local heat transfer coefficient, Reynolds number and wetting fraction of liquid nitrogen are estimated to be 7.9%, 5.8% and 3.6% respectively.

3. Results and discussion

3.1. General observations

A series of air-jet heat transfer tests with no liquid nitrogen involved are initially performed for benchmark validation of the experimental method and for generating the heat transfer reference datum to which the air/liquid nitrogen mist jet results could be compared. Fig. 3 shows the typical heat transfer results for pure airflow impinging jets obtained at Reynolds number of 10,000 with separation distances of 6 and 8 jet diameters. Also

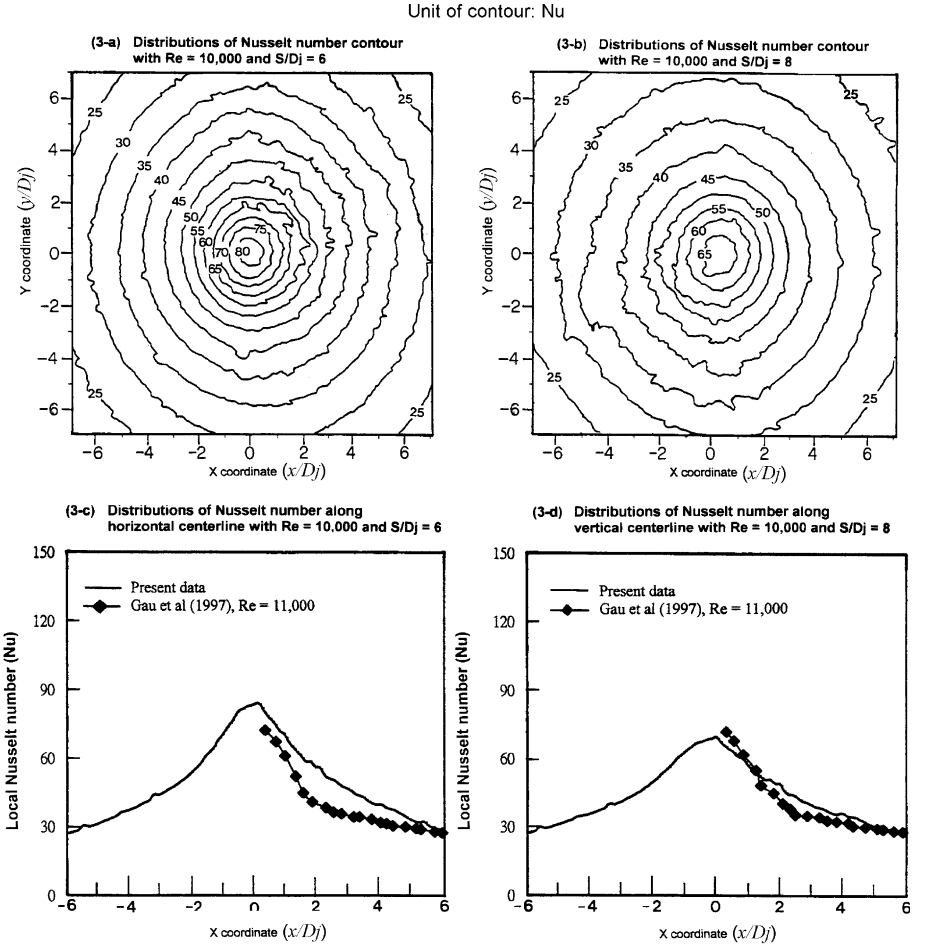

Fig. 3. Distributions of Nusselt number over impinging surface of air jet at Reynolds number of 10,000 with separation distances of 6 and 8 jet diameters.

compared in the plots of Fig. 3 are the comparable heat transfer data of Gau et al. [17]. The characteristic length selected to define the local Nusselt number follows the definition of Gau et al. [17], which is the hydraulic diameter of jet nozzle, D_j. As revealed from the plots in Fig. 3, the distributions of heat transfer are symmetrical about the stagnation point. The increase of separation distance from 6 to 8 jet diameters reduces the overall heat transfer levels. The most effective cooling areas for pure air-jet test results only cover about 3–5 jet diameters of radial distance centered from the stagnation point, which agrees with the results of Kim and Camci [18]. Good agreements in the radial heat transfer variation between the present data and the results of Gau et al. [17] are observed. Over the entire range of Reynolds numbers and separation distances studied, the stagnation-point Nusselt number for impinging air jet are well correlated with $Re^{0.5}$, and 98% of the present stagnation Nusselt number data, Nu_S^A, are found to agree with ±11% of the present correlation defined in Eq. (4):

$$Nu_S^A = Re^{0.5} \times (1.044 - 0.4319e^{0.2601S/D_j}) \quad (4)$$

Comparing the present data correlated by Eq. (4) with Kim and Camci [18] and the correlative data of Vader et al. [19] indicated in Fig. 4, shows good agreements and that the normalized stagnation Nusselt number decreases monotonically with separation distance. Note that the correlation of Vader et al. [19] is derived from the water jet experiments, which writes $Nu_S = 0.28Re^{0.58} \times Pr^{0.4}$. As the correlative data of Vader et al. [19] fall closely with the correlating curve of Eq. (4) that reasonably converges all the results of present study and Kim and Camci [18] of impinging air jets in the S/D_j range of $2 \leqslant S/D_j \leqslant 10$, the value of 0.4 for the Prandtl number exponent could be a suitable functional structure to correlate the stagnation Nusselt number of impinging jet.

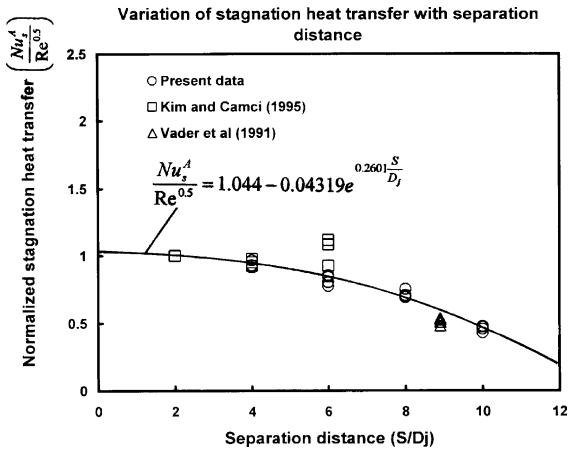

Fig. 4. Variation of normalized stagnation Nusselt number with separation distance.

The convective flow of high-momentum radial mist jet, accompanied with the suspended boiling mechanism of liquid nitrogen droplets in mist spray, could induce the locally low pressure to assist the evaporation processes in the mist jet and at the air/liquid nitrogen interface. Also the evaporative/boiling process of liquid nitrogen scattering in the mist jet could modify the flow and turbulence structures of the mist-jet flow. It becomes difficult to precisely account for the local fluid properties of the air–nitrogen mixture in order to define the dimensionless parameters such as the Nusselt number and Reynolds number. The overall heat transfer performance is alternatively leveled in terms of heat transfer coefficient, h, defined in Eq. (3). When the governing parameters such as the air jet Reynolds number, the mass fluxes of air and liquid nitrogen, the separation distance and the overheat at stagnation point are selected, the flow condition could be reproduced to generate a representative spatial heat transfer distributions over the impinging surface. The air-jet Reynolds number for both air and mist jets is evaluated in accordance with the airflow conditions and properties at the temperature level of air plenum. The test results generated at a predefined air-jet Reynolds number with and without liquid nitrogen are compared to reveal the heat transfer modifications due to the presence of liquid nitrogen droplets in the mist jet.

Fig. 5 shows the comparison of heat transfer contours between the results of air/liquid nitrogen mist jet and pure air jet at Reynolds number of 20,000, which reveals the typical influences of impinging mist jet on the distribution pattern of heat transfer coefficients over the impinging surface. As shown, the distributions of heat transfer contour over the impinging surface are symmetrical about two axes of $X = 0$ and $Y = 0$ for air jet but are only symmetrical about the vertical axis of $X = 0$ for the air/liquid nitrogen mist jet. The broken symmetry about the horizontal centerline is caused by the enhanced influences of earth gravity on the vertical momentum balance of mist jet when the liquid nitrogen droplets are involved. It is observed from the thermal image of the impinging surface and the photographs of mist spray as typified in Fig. 2b that the horizontal jet trajectory is bent downward when the air/liquid nitrogen mist jet is tested. A consequent earth gravity effect is to drive the radial convective mist flow and the liquid nitrogen film-flow downward so that the oval-shaped heat transfer contours are developed on the impinging surface of air/liquid nitrogen mist jet. At the central region of $-1.5 \leqslant X \leqslant 1.5$ and $-2.5 \leqslant Y \leqslant 2$, the convective coefficient distributions are quite uniform. When the supply of liquid nitrogen is sufficient to establish a liquid film in this core region, the motion of fluid activated by

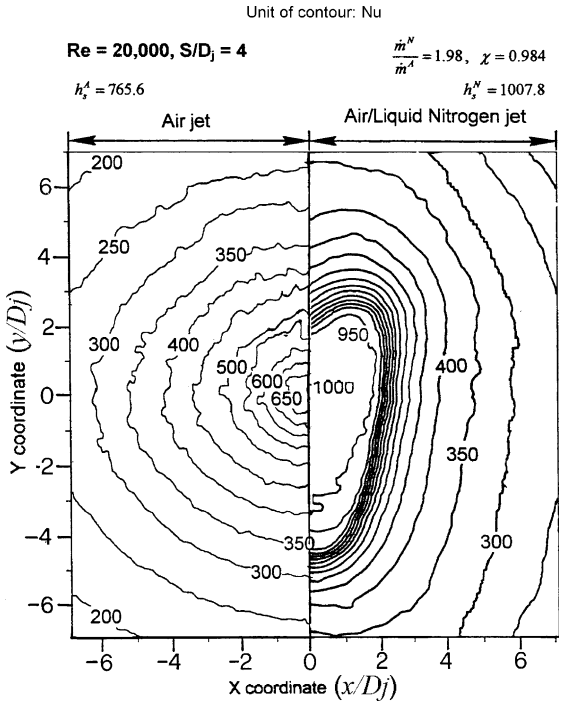

Fig. 5. Comparison of heat transfer contours over impinging surface between air jet and air–N_2 jet with jet Reynolds number of 20,000 and separation distance of $4S/D_j$.

the boiling on the superheated surface is vigorous. The state of convective boiling over this central wetting region hardly changes even if the spatially varied forced convection is applied to the bulk radial mist flow. In this central core regime, most of the heat transferred from the superheated surface is spent to cover the latent heat of evaporation. An active, self-supporting boiling layer is kept on this core heated surface, over which an upper liquid film is covered, and from which the splash of droplets is produced due to the ejection of vapor jets from the underlying boiling layer [20]. Boiling induced mixing and the latent energy of phase change dominate the overall heat removal capability in this wetting core region, while the influence of bulk-stream hydrodynamics and the droplet impacting mechanism are essentially negligible. This result agrees with the previous study on the water jet impingement boiling heat transfer, in which Wolf et al. [21] reported that the streamwise distance from the stagnation line influences heat transfer predominantly in the single phase convection regime but has no appreciable effect on the fully developed nucleate boiling. Immediately adjacent to the central core region where the heat transfer coefficients are uniformly distributed is a narrow ring-shaped band within which very dense distributions of heat transfer contour are observed. This narrow ring encapsulates the uniformly distributed heat transfer core across which the heat transfer coefficient rapidly transits from the wetting regime of complete evaporation to the non-wetting rebound regime. Note that, as the impinging surface is heated by a uniform heat flux, the reduction of overall convective coefficient, h, away from the central core region, as shown in Fig. 5, results in the radial increase of wall temperature and consequently the overheat. Therefore, when the radial distance from the stagnation point increases over the transition narrow ring, the liquid nitrogen droplets could bounce back upon impaction due to the formation of a vapor cushion. In this so-called non-wetting rebound regime, the splashing becomes very violent that hardly keeps an upper layer liquid film so that the heated surface could expose to the radial mist flow, yielding a considerable reduction in heat transfer from the wetting core regime. The gradually radial heat transfer reduction in the non-wetting rebound regime is observed when the radial distance from the narrow ring regime increases so that the heat transfer is predominated by the single-phase convection. The increase in h over this non-wetting rebound regime from the pure air-jet reference, as compared in Fig. 5, is partly due to the influences of suspended boiling of liquid nitrogen on the turbulence and vorticity of free stream bulk flow. The spatial variations in boiling layer and liquid film result in three distinct heat transfer regimes; namely the central wetting regime, the rapid transition regime, and the non-wetting rebound regime where the fully developed boiling, the partial boiling, and the forced convection of radial flow, respectively, dominate the heat transfer mechanism.

3.2. Effects of $\frac{\dot{m}^N}{\dot{m}^A}$, S/D_j and Re

Fig. 5 reveals that the interactive mechanisms of evaporation/boiling process of liquid nitrogen and bulk convection of mist flow, which are mutually influenced, could generate three distinct heat transfer regimes over a superheated impinging surface. With the boundary conditions specified by the present experimental rig, the strategy is initially formulated in Eq. (5) as:

$$h(X,Y) = \Psi\left\{ Re, S/D_j, \frac{\dot{m}^N}{\dot{m}^A} \right\} \tag{5}$$

where Ψ is the unknown function to be identified. The isolated effect in association with each controlling parameter of Eq. (5) is revealed by systematically varying one parameter with the remaining parameters controlled at constants. Fig. 6 shows the isolated effect of mass flow ratio, $\frac{\dot{m}^N}{\dot{m}^A}$, at Reynolds number of 10,000 and separation distance of six jet diameters. Because the Reynolds number remains constant, the mass flow rate of airflow and the momentum of the mist jet that induces the entertainment are approximately fixed for all three

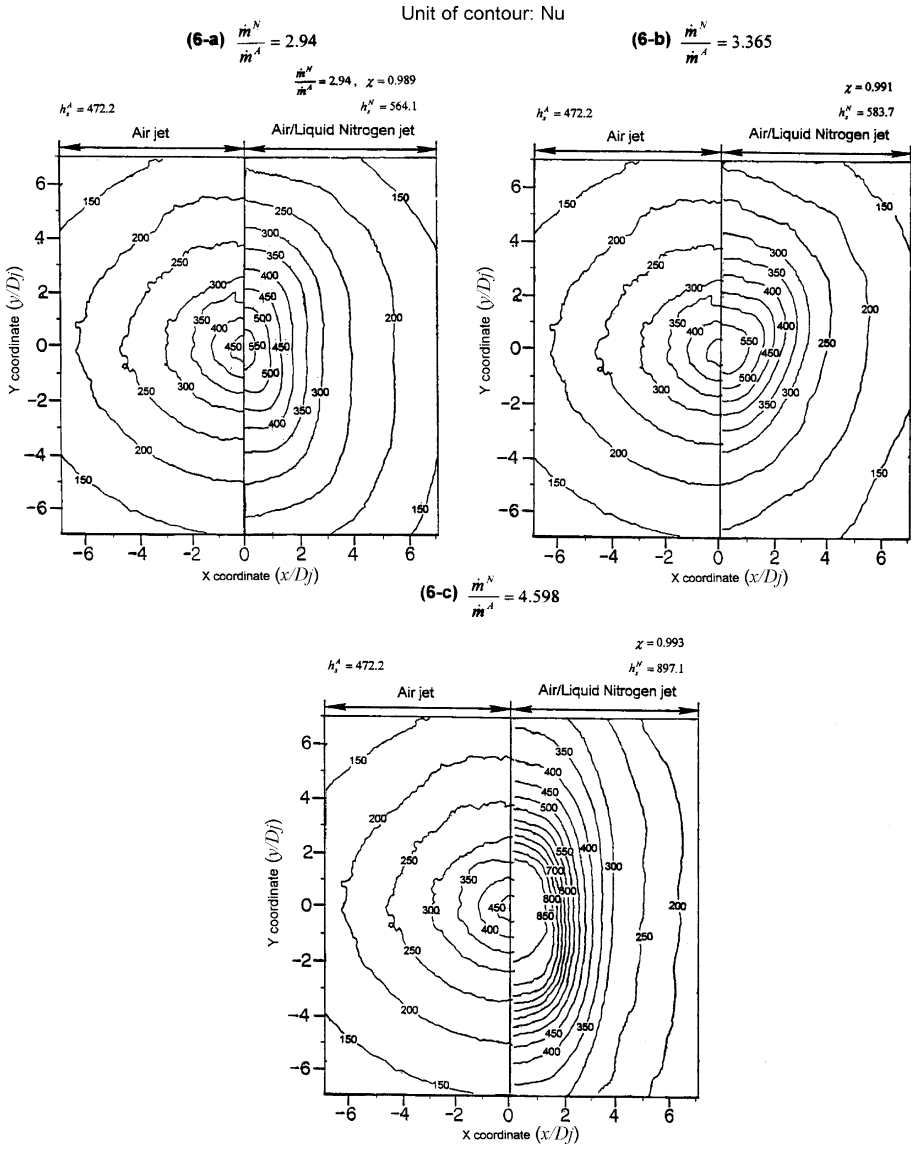

Fig. 6. Effect of mass flow ratio of liquid nitrogen to airflow on heat transfers at jet Reynolds number of 10,000 and separation distance of 6 S/D_j.

heat-transfer scenarios compared in Fig. 6. In this case, the increased mass flow ratio, $\frac{\dot{m}^N}{\dot{m}^A}$, results in the increases of liquid nitrogen flux and the droplet size [22]. As the previous study [2] demonstrated that the dense spray heat transfers were not much dependent on the droplet diameter and velocity, the most significant factor responsible for the variations in heat transfers due to the change of mass flow ratio, $\frac{\dot{m}^N}{\dot{m}^A}$, illustrated in Fig. 6 is considered as the mass flux of liquid nitrogen. As shown in Fig. 6, the increase of mass flux of liquid nitrogen consistently enhances the stagnation heat transfer that is accompanied with the gradual development of central wetting regime. When the mass flow ratio, $\frac{\dot{m}^N}{\dot{m}^A}$, increases from 2.94 toward 4.598, the distributions of overall heat transfer coefficient evolve from the complete non-wetting rebound regime (see Fig. 6a) towards the three-regime pattern (see Fig. 6c). The transition regime emerges once the central wetting region is established. Without the development of compact liquid film around the stagnation point, the transition regime is not clearly observed (see Fig. 6a and b). The influences of mass flow ratio, $\frac{\dot{m}^N}{\dot{m}^A}$, on heat transfer are weakened apart from the central core region. The variation of mass flow ratio, $\frac{\dot{m}^N}{\dot{m}^A}$, only causes small heat-transfer differences between the

three illustrative examples compared in Fig. 6 in the spatial regions of $X \geqslant 4$ and $Y \geqslant 5$ and $X \leqslant -4$ and $Y \leqslant -5$, even though the heat transfer enhancements from the pure air-jet counterparts still remain.

Fig. 7 compares the overall heat transfer performances with different separation distances at Reynolds number of 10,000 and mass flow ratio, $\frac{\dot{m}^{N}}{\dot{m}^{A}}$, about 4.55 to show the effect of separation distance on heat transfer in isolation. In this case, the mass fluxes of airflow and liquid nitrogen flow remain constant. Having the separation distance increased, the mist-jet fluids are slowed down when they entrain surrounding atmosphere that could lead to insufficient impacting momentum for droplet to penetrate the vapor layer at the superheated surface. The more the separation distance is, the less momentum in the horizontal trajectory of mist jet possesses. With the increased entrainment, the wetting factor of mist jet is reduced. These two factors in combination cause the heat transfer differences between the plots revealed in Fig. 7. The increase of separation distance from 4 to 10 jet diameters causes the heat transfer distributions varying from the three-regime pattern (see Fig. 7a and b) towards the complete non-wetting rebound regime (see Fig. 7d). A pattern of transition

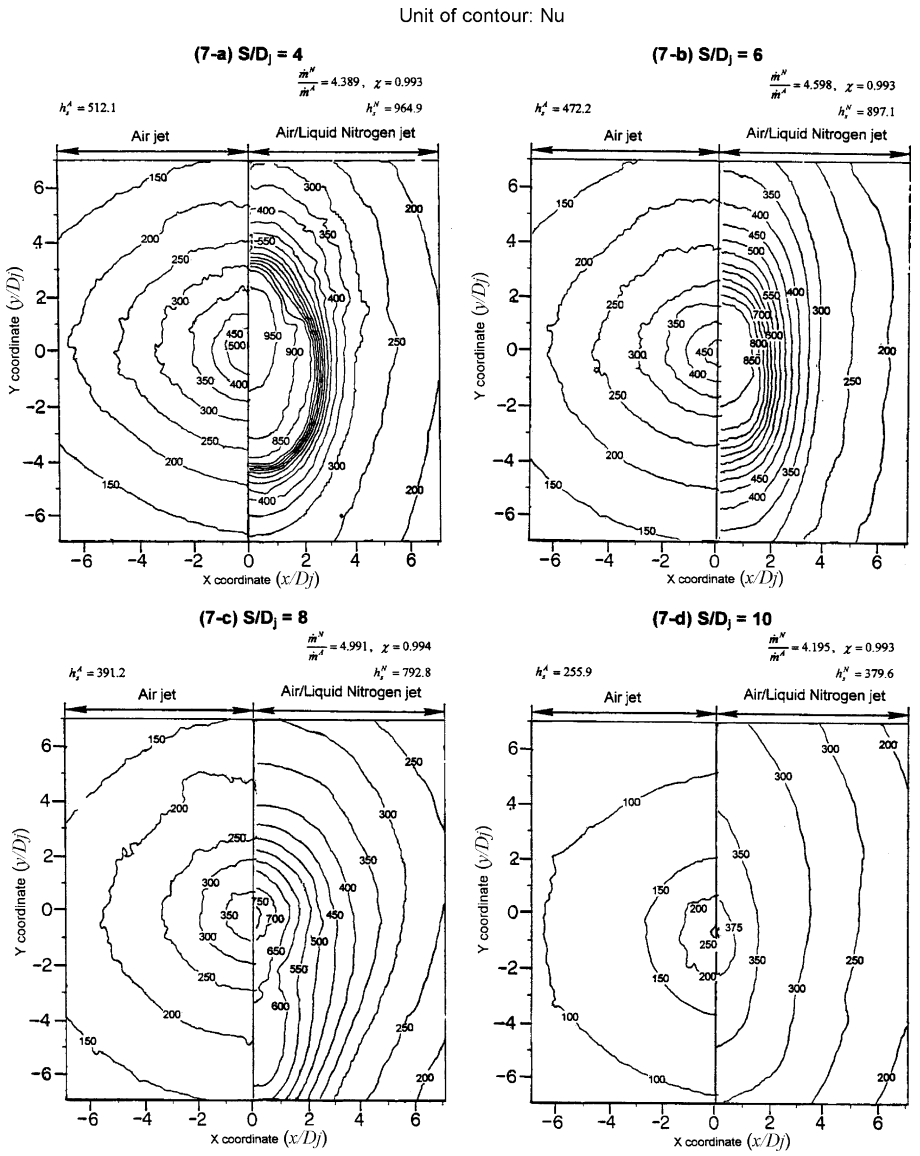

Fig. 7. Effect of separation distance on heat transfers with jet Reynolds number of 10,000 and mass flow ratio of liquid nitrogen to airflow of 4.55.

between the three-regime pattern and complete non-wetting rebound regime is typified in Fig. 7c. At separation distance of 4 jet diameters, the development of central wetting regime with compact liquid nitrogen film is clearly shown. The narrow ring encapsulating the central core regime rapidly transits the convective boiling heat transfer level from the central wetting regime toward the single-phase convective flow level in the complete non-wetting rebound regime. When the separation distance increases from 4 to 6 jet diameters, the ring of transition expands and the central wetting regime shrinks (compare Fig. 7a and b). This observation mainly reflects the effects of weakened droplet impacting momentum on the development of liquid film. The convective boiling in associated with the development of liquid film is moderated, while the region where the partial boiling dominates heat transfer is extended. Instead of a rapid transition into the non-wetting rebound pattern (see Fig. 7a), the reduced impacting momentum of droplet slows down such transition (see Fig. 7b). A further increase of separation distance from 6 to 8 jet diameters (compare Fig. 7b and c), which reduces the impacting momentum of droplet further, causes a continuous expansion of the transition regime. The heat transfer characteristic of central wetting regime disappears. However, with the extension of partial boiling region, the heat transfer physics in the complete non-wetting rebound regime is partly replaced by the partial boiling. Heat transfer levels in the spatial range of $6 > X > 3$ (see Fig. 7c) are thus higher than those counterparts obtained with separation distances of 4, 6 and 10 jet diameters (see Fig. 7a, b and d). At separation distance of 10 jet diameters (see Fig. 7d), the heat transfer distributions show the typical pattern of complete non-wetting rebound regime where the forced convective radial flow dominates the overall heat transfer performance. A systematic increase of stagnation heat transfer level with the reduction in separation distance is also indicated in Fig. 7.

When the isolated effects of $\frac{\dot{m}^{N}}{\dot{m}^{A}}$ and S/D_j are examined in the manners described in Figs. 6 and 7 respectively, the change of $\frac{\dot{m}^{N}}{\dot{m}^{A}}$ or S/D_j does not incur any simultaneous variation in the other physical manifestations governed by the remaining parameters of Eq. (5). When the Reynolds number is systematically increased at fixed value of mass flow ratio, $\frac{\dot{m}^{N}}{\dot{m}^{A}}$, the mass flux of liquid nitrogen is correspondingly increased in order to keep the mass flow ratio, $\frac{\dot{m}^{N}}{\dot{m}^{A}}$, unchanged. The variation of Reynolds number at a selected mass flow ratio, $\frac{\dot{m}^{N}}{\dot{m}^{A}}$, thus incurs twofold modifications, namely the change of mass flux of liquid nitrogen and the variations in the mechanisms associated with air-jet Reynolds number, such as the free-stream turbulence, the entrainment, the convective bulk flow and the droplet momentum. Fig. 8 shows the isolated *Re* effect on heat transfer at separation distance of 6 jet diameters with the mass flow ratio, $\frac{\dot{m}^{N}}{\dot{m}^{A}}$, controlled at about 2.78. As shown in Fig. 8, heat transfers over the entire superheated surface increase with the increased Reynolds number. Note the systematic increase of heat transfer in the non-wetting rebound regime of $-4 \geqslant X$ and $X \geqslant 4$ shown in Fig. 8 when Reynolds number gradually increases. Inferring from the systematic variation of heat transfer coefficient with Reynolds number, heat transfers in the non-wetting rebound regime are strong functions of Reynolds number. This statement applies for all the test results with $S/D_j \leqslant 8$, which will be further illustrated in the following section. The distributing pattern of heat transfer contours gradually evolves from the non-wetting rebound regime into the three-regime pattern when Reynolds number increases from 5000 to 20,000. As seen in Fig. 8a and b, the central wetting regime is not well established at Reynolds number of 5000 and 10,000 due to the lack of droplet momentum and the insufficient supply of liquid nitrogen from the mist jet. When Reynolds number increases from 10,000 to 15,000, the central wetting regime is established (see Fig. 8c) and the three-regime pattern of heat transfer distribution is observed. Further increase of Reynolds number from 15,000 to 20,000 causes a continuous heat transfer enhancement over the entire superheated surface. Note the central wetting regime and the transition ring are both shrunk toward the stagnation point when Reynolds number increases from 15,000 to 20,000 (compare Fig. 8c and d).

The comparison of wall temperature data from the thermal images of Fig. 8c and d confirms the lower wall temperature levels at Reynolds number of 20,000. It is these lower wall temperatures and the slight increase in heat flux that results in the increased heat transfers from the results obtained at Reynolds number of 15,000 (compare Fig. 8c and d). In general, the increased mass flux of liquid nitrogen and the enhanced momentum of droplet gained from the mist-jet stream due to the increase of Reynolds number could produce more rigorous impacting dynamics between droplets and with superheated wall/liquid film. In [3], the velocity profiles of wall-jet flow with gaseous phase reveal a wall-jet emanating radially outward from the spray impingement region, near the front of which there is a vortex. This vortex structure influences the radial movement of droplets. Due to the interaction of turbulent mist flow resulting from the enhanced air entrainment when the wall vortex moves radially with the higher convective velocity over the high temperature wall, the radial velocities of wall-jet flow are higher than those counterparts with lower temperature wall [3]. Also the liquid film is thicker for the low temperature wall [3]. In addition, the flow visualization results obtained using the conventional photographic technique show that the spread angles of mist sprays increase with the increased Reynolds number as demonstrated in Fig. 2b. As the spread angle at Reynolds number of 20,000 is increased

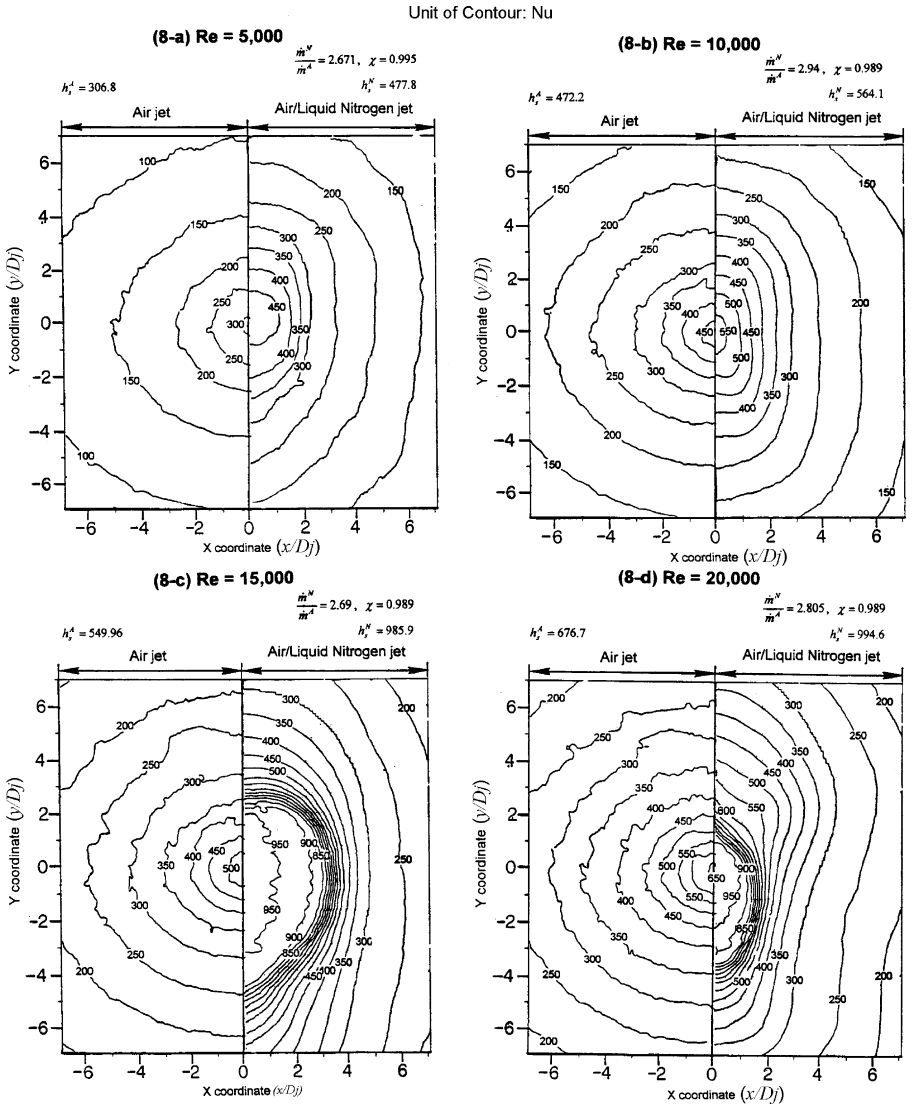

Fig. 8. Effect of jet Reynolds number on heat transfers with separation distance of 6 S/D_j and mass flow ratio of liquid nitrogen to airflow of 2.78.

from the scenario found at Reynolds number of 15,000, the jet momentum of mist jet is diffused with wider range due to the larger spread angle at higher Reynolds number. It is likely that the shrinkage of wetting and transition regimes found in Fig. 8d is directly related with the lower radial velocities of wall-jet flow over the cooler wall. This weakened radial inertia interacts with earth gravity to affect the radial distributions of mass and momentum in the wall-jet flow, which produces the heat transfer distributions shown in Fig. 8d.

With varied overall convective capability by adjusting Re, S/D_j and/or $\frac{\dot{m}^N}{\dot{m}^A}$, the wall temperatures are correspondingly modified. Using Fig. 8d as an illustrative example, the modified wall temperature distributions could sometimes considerably affect the heat transfer distributions over the impinging superheated surface. It is the interactions between mist jet, wall temperature and two-phase wall-jet flow that create the inter-correlation between the parameters of $\frac{\dot{m}^N}{\dot{m}^A}$, S/D_j and Re. These interactive influences between $\frac{\dot{m}^N}{\dot{m}^A}$, S/D_j and Re could be better illustrated in the manner described in Fig. 9. Note, in order to highlight the effectiveness of impinging air/liquid nitrogen mist jet on heat transfer enhancements, the heat transfer rates, h^N, for the mist-jet results are normalized by the pure air-jet counterparts, h^A. The variations of heat transfer ratio, $\frac{h^N}{h^A}$, along the vertical

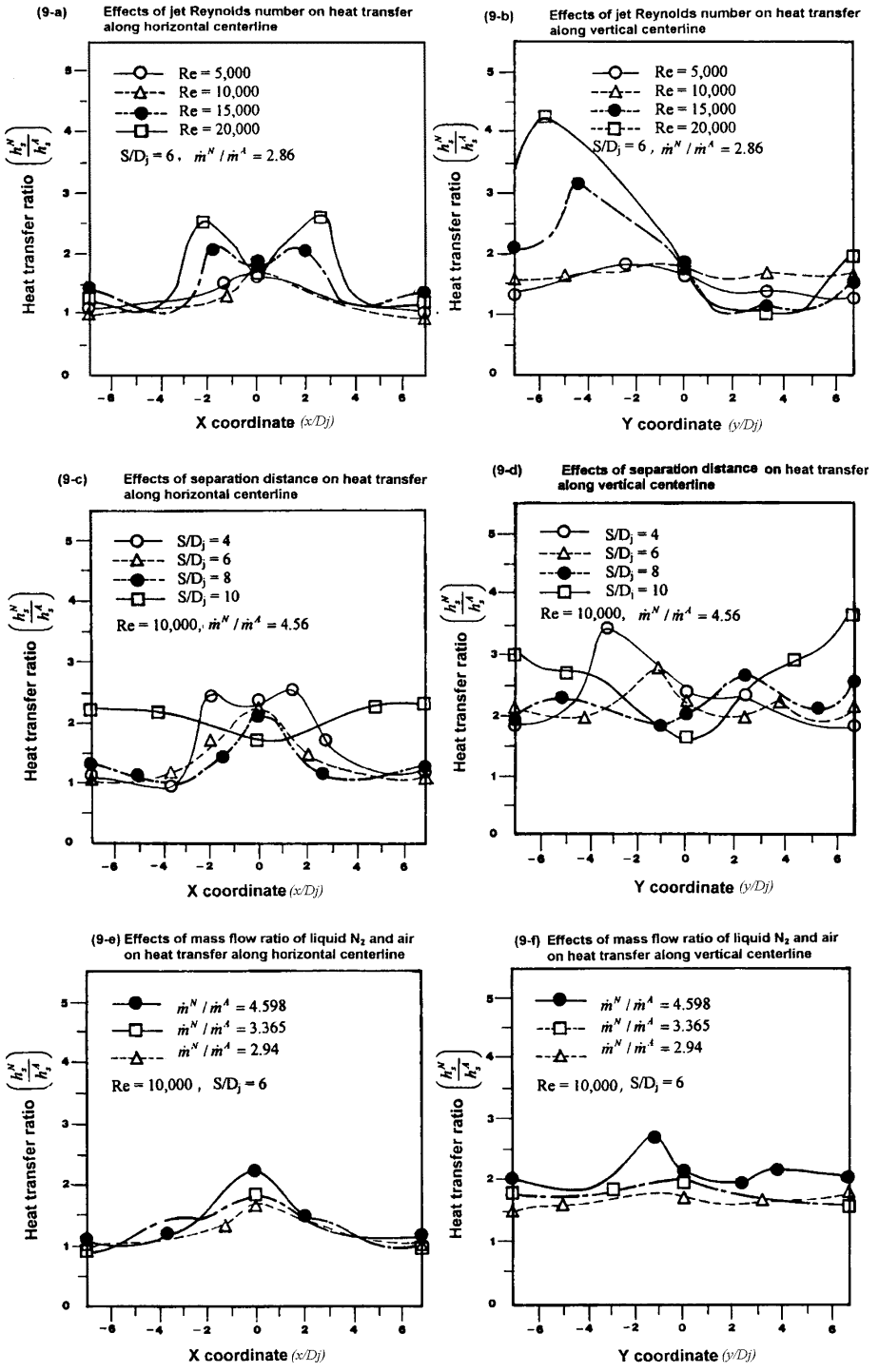

Fig. 9. Effects of jet Reynolds number, separation distance and mass flow ratio of liquid N_2 and air on normalized heat transfer along vertical and horizontal centerlines of impinging surface.

and horizontal centerlines, summarized from test results shown in Figs. 6–8, are plotted in Fig. 9. The influences of each controlling parameter summarized in equation (5) in isolation along the horizontal and vertical centerlines of the impinging surface are examined by plotting the normalized heat transfer results along two axes

of $X = 0$ and $Y = 0$. In the regions of $X \leqslant -4$ and $X \geqslant 4$, the heat transfer ratios are close to unity (see Fig. 9a, c and e) that assures the development of non-wetting rebound regime, except for the results obtained at separation distance of 10 jet diameters (see Fig. 9c). In the central wetting regime of $-4 \leqslant X \leqslant 4$, the variations of normalized heat transfer are symmetrical about the vertical centerline. The higher heat transfer enhancement in the central core region is attributed to the additional heat absorption for the latent heat of liquid nitrogen. The dimple with local minimum at stagnation point due to the higher heat-transfer increasing rate toward the stagnation point of air jet is found at Reynolds numbers of 15,000 and 20,000 in Fig. 9a and with separation distances of 4 and 10 jet diameters in Fig. 9b. Except the case with separation distance of 10 jet diameters, the heat transfer variations along horizontal centerline that involve dimple are those results with liquid film established in the central core region, where the heat transfer rates distribute uniformly (see Figs. 7a and b and 8c and d). For the case of $S/D_j = 10$ shown in Fig. 9c, the heat transfer increments about 100% of air-jet levels distribute rather uniformly along the horizontal centerline. In addition to the overall heat transfer improvements obtained at separation distance of 10 jet diameters (see Fig. 9c), a dimple with local minimum at stagnation point is generated due to the higher increasing rate in heat transfer toward the stagnation point of air jet. The heat transfer improvements with $S/D_j = 10$ indicate the involvement of evaporation and/or boiling process that scatters over the scanned heating area. As illustrated previously, the increase of separation distance slows the mist-jet fluids when they entrain surrounding atmosphere and extends the radial range under the spray cone upon impaction. A net result of increasing separation distance to 10 jet diameters under the conditions specified in Fig. 9c is the radial extension of droplet-spread that accompanies with the insufficient impacting momentum of droplet for penetrating the vapor layer at the superheated surface. Therefore there is no indication shown in Fig. 7d that the liquid nitrogen film is developed. In this case, the partial boiling prevails over the entire scanned area at separation distance of 10 jet diameters (see Fig. 9c).

Most of heat-transfer variations along the vertical centerline (see Fig. 9b, d and f) show asymmetric distributions about the horizontal centerline with the better cooling performances developed in the bottom half of scanned area. This asymmetry in heat transfer distributions reflects the influences of earth gravity on heat transfer. Note the gravity could not cause distinguishable effect on heat transfers over the impinging surface of single-phase air jet within the experimental conditions tested. When heat transfers along vertical centerline showed in Fig. 9b, d and f compare with their counterparts along the horizontal centerline, the heat transfer improvements in the regions of $Y \leqslant 0$ and $Y \geqslant 0$ are, respectively, enhanced and suppressed from the symmetrical results showed in Fig. 9a, c and e, except the case of $S/D_j = 10$ in Fig. 9c and d. This is mainly due to the gravity effects which, respectively, reduce and enhance the radial momentum of wall-jet flow in the regions of $Y \geqslant 0$ and $Y \leqslant 0$. The most significant gravity effects on heat transfer are found for the cases of Re = 15,000 and 20,000 in Fig. 9b, $S/D_j = 4$ in Fig. 9d and $\frac{\dot{m}^N}{\dot{m}^A} = 4.598$ in Fig. 9f, which results share a common feature of developed central wetting regime over the impinging surface. It is felt that the considerable heat transfer improvements developed in the bottom half of scanned area for these three flow conditions are due to the increased supply of liquid nitrogen from liquid film driven by the downward gravity force. Based on the data trends shown in Fig. 9b, d and f, the increase of Reynolds number or mass flow ratio, $\frac{\dot{m}^N}{\dot{m}^A}$, or the decrease of separation distance increases the degree of asymmetry about horizontal centerline and therefore enhances the gravity effects on heat transfer. It is also noticed in Fig. 9d that the distributing pattern of $S/D_j = 10$ follows the symmetrical pattern found in Fig. 9c. The implications of symmetries about both vertical and horizontal centerlines with separation distance of 10 jet diameters shown in Fig. 9c and d are the weakened gravity effect on near-wall flow phenomena and the improved homogeneity of droplet scattering in the mist jet.

The variation of each controlling variable such as *Re*, S/D_j, and $\frac{\dot{m}^N}{\dot{m}^A}$ with the other parameters remained constants creates various degrees of data spread in heat transfer ratio, $\frac{h^N}{h^A}$, at each X and Y locations shown in Fig. 9, except at the stagnation point shown in Fig. 9a and b. The variation of *Re*, S/D_j, or $\frac{\dot{m}^N}{\dot{m}^A}$ under the uniform heat flux heating condition has caused variations in wall temperature and consequently the degree of overheat over the heated surface, except at the stagnation point. The various degrees of data-spread generated at different X and Y locations shown in Fig. 9 are partly contributed from the differences in the degree of overheat. Nevertheless, as exemplified in Fig. 9a and b, the heat transfer ratios, $\frac{h^N}{h^A}$, obtained with different Reynolds numbers converge into a tight data-band at the stagnation point where the degree of overheat is controlled at 180 °C. Note the adjustment of Reynolds number at fixed mass flow ratio, $\frac{\dot{m}^N}{\dot{m}^A}$, and separation distance incurs simultaneous variations in mass flux of liquid nitrogen and mist-jet momentum. The collapsed data at the stagnation point revealed in Fig. 9a and b implies the possibility of isolating the combined effects in association with these two physical manifestations controlled by Reynolds number. A subsequent review of the entire data generated ensures that the heat transfer ratios, $\frac{h^N}{h^A}$, obtained with different Reynolds numbers but at the fixed values of $\frac{\dot{m}^N}{\dot{m}^A}$ and S/D_j are converged into tight data bands at the stagnation point. This result confirms the

possibility of isolating *Re* effects from $\frac{\dot{m}^{N}}{\dot{m}^{A}}$ and S/D_j effects that has led to a simplified structure of Ψ function in Eq. (5).

3.3. Stagnation heat transfer

Fig. 10 summarizes the entire stagnation heat transfer data generated in terms of heat transfer ratio, $\frac{h_s^N}{h_s^A}$. At each separation distance (see each plot of Fig. 10), the increase of mass flow ratio, $\frac{\dot{m}^N}{\dot{m}^A}$, continuously improves

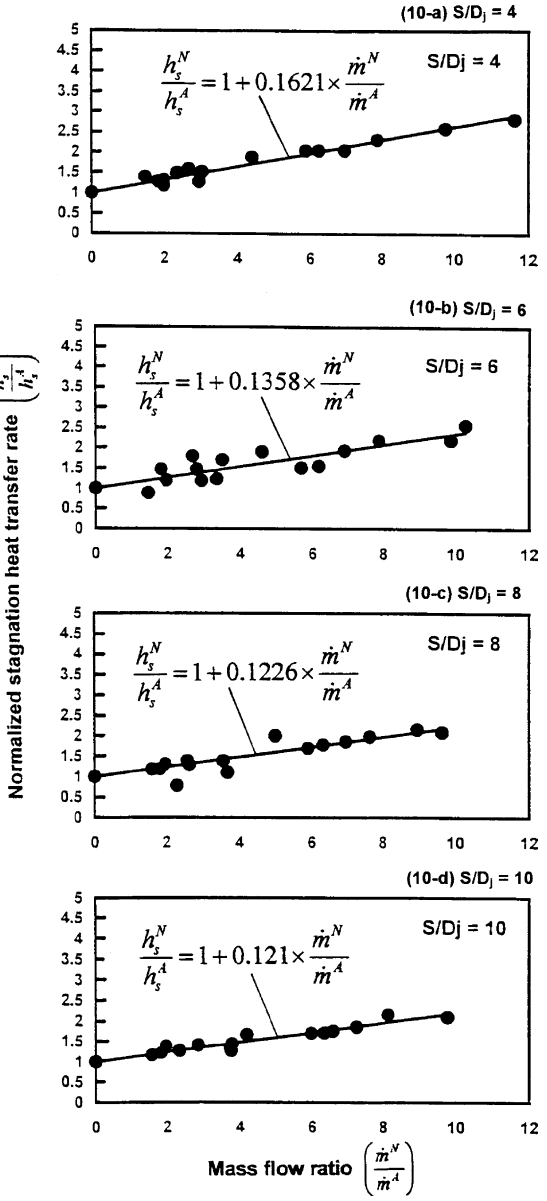

Fig. 10. Variations of normalized stagnation heat transfer with mass flow ratio of liquid nitrogen to airflow at fixed S/D_j.

stagnation heat transfer. The zero asymptotic heat transfer solution in each plot of Fig. 10 resembles the pure air-jet stagnation heat transfer level. A linear correlating line indicated in each plot of Fig. 10 could reasonably describe the data trend observed. Note the convergence of data generated with all Reynolds numbers into a tight data trend as shown in Fig. 10 suggests that the normalized stagnation heat transfer could be correlated into a single variable function of mass flow ratio, $\frac{\dot{m}^N}{\dot{m}^A}$, when the separation distance remains constant. A physical implication of such data-collapsing tendency shown in each plot of Fig. 10 is the approval for isolating *Re* effects from the physical consequences dominated by the parameters of $\frac{\dot{m}^N}{\dot{m}^A}$ and S/D_j. Led by the observation of all S/D_j versions of Fig. 10 and the physical constraint that the normalized heat transfer, $\frac{h_s^N}{h_s^A}$, has to be unity when the mass flow ratio, $\frac{\dot{m}^N}{\dot{m}^A}$, is zero, it is proposed that $\frac{h_s^N}{h_s^A}$ can be reasonably well approximated by the equation of the following general form:

$$\frac{h_s^N}{h_s^A} = 1 + \xi(S/D_j) \times \frac{\dot{m}^N}{\dot{m}^A} \tag{6}$$

where the ξ is function of dimensionless separation distance, S/D_j. These correlated ξ functional values are then examined in order to determine the functional shape of ξ function over the range of separation distance tested. It is found that the increase of separation distance decreases the value of ξ function, which reflects the weakened $\frac{\dot{m}^N}{\dot{m}^A}$ effects on heat transfer when separation distance increases. The data of ξ function in the range of $4 \leqslant S/D_j \leqslant 10$ is well represented by an exponential-type curve fit given by

$$\xi = 0.1811 \times e^{-0.0405 S/D_j} \tag{7}$$

An attempt has been made to experimentally uncouple these effects via a systematic experimental strategy together with a detailed analysis of the resulting derived stagnation heat transfer data. The outcome has been an empirical equation, which could be used to estimate stagnation heat transfer. This proposal is embodied in Eq. (8):

$$\frac{h_s^N}{h_s^A} = 1 + \left(0.1811 \times e^{-0.0405 \frac{S}{D_j}}\right) \times \frac{\dot{m}^N}{\dot{m}^A} \tag{8}$$

The overall success of this proposal is indicated in Fig. 11 where the entire stagnation heat transfer data are compared with the correlative predictions evaluated by Eq. (8). The maximum discrepancy of ±20% between the experimental and correlating results is achieved for 95% of the entire data generated at the stagnation point. The range of variations in normalized stagnation heat transfer, $\frac{h_s^N}{h_s^A}$, is 1.2–2.8 as shown in Fig. 11. Heat transfer improvements with the present parametric conditions tested are acquired. Justified by the achieved accuracy, Eq. (8) could provide the reasonable stagnation heat

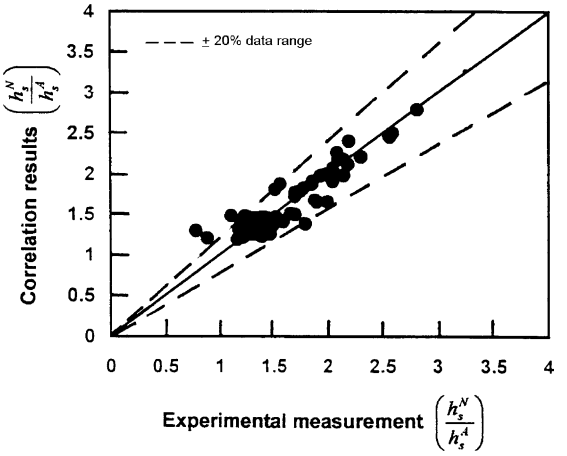

Fig. 11. Comparison of correlative predictions with experimental measurements of normalized stagnation heat transfer.

transfer evaluation to assist the design initiative of the instant freezing facility using impinging air/liquid nitrogen mist jet.

4. Conclusions

This paper has described a detailed experimental program undertaken to examine the interactive effects of jet Reynolds number, mass flow ratio of liquid nitrogen to airflow and separation distance on heat transfer of an impinging air/liquid nitrogen mist jet with overheat of 180 °C at stagnation point. The impacting momentum of liquid nitrogen droplet, which is Re and S/D_j dependent, affects the capability of penetrating boiling vapor layer and therefore the development of liquid film; while the mass flux of liquid nitrogen crucially influences the physics of evaporative wetting. As well as re-confirming the fact that Re, S/D_j and $\frac{\dot{m}^N}{\dot{m}^A}$ interactively have a significant influence on the two-phase impinging jet convection, the following important points have been identified.

1. When the jet momentum and supply of liquid nitrogen are sufficient to penetrate the boiling vapor layer that leads to the development of a surface liquid film, three distinct heat transfer regimes, namely the central wetting regime, rapid transition regime and non-wetting rebound regime, are coherently jointed over impinging surface. The narrow oval shaped transition ring, within which very dense distributions of heat transfer contour are resolved, encapsulates the uniformly distributed heat transfer wetting core that rapidly transits the enhanced heat transfer level from the wetting regime of complete evaporation to the level of non-wetting rebound regime.

2. The systematic increase of Re or $\frac{\dot{m}^N}{\dot{m}^A}$ improves heat transfers that is accompanied with a gradual development of central wetting regime. The increase of separation distance weakens droplet impacting-momentum and increases entrainment, which has led to the expansion and shrinkage of transition and central wetting regimes respectively. A further increase of separation distance could lead to the development of non-wetting rebound regime over the entire superheated surface where the forced convective radial *mist-flow* dominates heat transfer.

3. With liquid nitrogen film established over the central core region, a local minimum in heat transfer enhancement develops at stagnation point due to the higher heat transfer increasing-rate toward the stagnation point of air jet. Owing to the gravity effects on radial momentum of wall-jet flow and liquid film, heat transfer enhancements along the vertical centerline are, respectively, enhanced and suppressed from the counterparts of symmetrical distributions along the horizontal centerline in the regions of $Y \leqslant 0$ and $Y \geqslant 0$. The increase of Re or $\frac{\dot{m}^N}{\dot{m}^A}$, or the decrease of S/D_j increases the degree of asymmetry about horizontal centerline and thus enhances the gravity effects.

4. If the relative change in stagnation heat transfer is expressed as a ratio of the heat transfer rate obtained with air/liquid nitrogen jet to that obtained with pure air jet and the same Reynolds number, then that ratio has a strong tendency to be independent of jet Reynolds number. This result is true in the ranges of mass flow ratio of liquid nitrogen to airflow and separation distance tested and is an important experimental observation since it could simplify the quest for a correlating equation along the line of Eq. (5).

5. The proposed correlations for stagnation heat transfers of pure air jet and air/liquid nitrogen mist jet are physically consistent and permit the individual effects of Re, S/D_j and $\frac{\dot{m}^N}{\dot{m}^A}$ to be taken into account. Within the present parametric conditions tested, the stagnation heat transfer enhancement in terms of $\frac{h_s^N}{h_s^A}$ falls in the range of 1.2–2.8.

Acknowledgements

This work was financially supported by National Science Council, Taiwan, Republic of China, towards National Kaohsiung Institute of Marine Technology under grant number NSC-2212-E-022-002.

References

[1] C.O. Pederson, An experimental study of the dynamic behavior and heat transfer characteristics of water droplets impinging upon a heated surface, Int. J. Heat Mass Transfer 13 (1970) 369–381.

[2] S. Deb, S.G. Yao, Analysis on film boiling heat transfer of impacting sprays, Int. J. Heat Mass Transfer 32 (1989) 2099–2112.

[3] D.W. Stanton, C.J. Rutland, Multi-dimensional modeling of thin liquid films and spray–wall interactions resulting from impinging sprays, Int. J. Heat Mass Transfer 41 (1998) 3037–3054.
[4] S. Chandra, C.T. Avedisian, On the collision of a droplet with a solid surface, Proc. R. Soc. London, A 264 (1991) 15–41.
[5] B. Siwon, Experimental investigations of liquid film by a gas–liquid spray jet impinging onto a flat surface, Int. Commun. Heat Mass Transfer 20 (1993) 665–674.
[6] J. Yang, L.C. Chow, M.R. Pais, An analytical method to determine the liquid film thickness produced by gas atomized sprays, ASME J. Heat Transfer 118 (1996) 255–258.
[7] K.M. Graham, S. Ramadhyani, Experimental and theoretical studies of mist jet impingement cooling, ASME J. Heat Transfer 118 (1996) 343–349.
[8] S.W. Chang, L.M. Su, Heat transfer of confined impinging air–water mist jet, JSME Int. J. Ser. B 44 (2001) 274–287.
[9] K.J. Choi, S.C. Yao, Mechanism of film boiling heat transfer of normally impacting spray, Int. J. Heat Mass Transfer 30 (1987) 311–318.
[10] M.R. Pais, L.C. Chow, E.T. Mahefkey, Surface roughness and its effects on the heat transfer mechanism in spray cooling, ASME J. Heat Transfer 114 (1992) 211–219.
[11] Yu.A. Buyevich, V.N. Mankevich, Interaction of a dilute mist flow with a hot body, Int. J. Heat Mass Transfer 38 (1995) 731–744.
[12] Yu.A. Buyevich, V.N. Mankevich, Cooling of a superheated surface with a jet mist flow, Int. J. Heat Mass Transfer 39 (1996) 2353–2362.
[13] H. Miyazaki, E.M. Sparrow, Analysis of effect of free-stream turbulence on heat transfer and skin friction, ASME J. Heat Transfer 99 (1977) 614–619.
[14] D.C. McCormick, F.L. Test, R.C. Lessman, The effect of free-stream turbulence on heat transfer from a rectangular prism, ASME J. Heat Transfer 106 (1984) 268–275.
[15] S. Polat, B. Huang, A.S. Mujumbar, W.J.M. Douglas, Numerical flow and heat transfer under impinging jets: A review, in: C.L. Tien (Ed.), Annual Review of Numerical Fluid Mechanics and Heat Transfer, vol. 2, Hemisphere Publishing Corp., 1989, pp. 157–197.
[16] Editorial Board of ASME Journal of Heat Transfer, Journal of Heat Transfer Policy on Reporting Uncertainties in Experimental Measurements and Results, ASME Journal of Heat Transfer 115 (1993) 5–6.
[17] C. Gau, W.Y. Sheu, C.H. Shen, Impingement cooling flow and heat transfer under acoustic excitations, ASME J. Heat Transfer 119 (1997) 810–817.
[18] K. Kim, C. Camci, Fluid dynamics and convective heat transfer in impinging jets through implementation of a high resolution liquid crystal technique, Int. J. Turbo Jet Engines 12 (1995) 1–12.
[19] D.T. Vader, F.P. Incropera, R. Viskanta, Local convective heat transfer from a heated surface to an impinging, planar jet of water, Int. J. Heat Mass Transfer 34 (1991) 611–623.
[20] M. Monde, Y. Katto, Burnout in a high-flux boiling system with an impinging jet, Int. J. Heat Mass Transfer 21 (1978) 295–305.
[21] D.H. Wolf, F.P. Incropera, R. Viskanta, Local jet impingement boiling heat transfer, Int. J. Heat Mass Transfer 39 (1996) 1395–1406.
[22] M.S. Jenkins, S.R. Story, R.H. Davies, Defining air-mist nozzle operating conditions for optimal spray cooling performance, Proceedings of the Nineteenth Australasian Chemical Engineering Conference, Newcastle, Australia, 1991, pp. 1062–1071.